Observation of double star by long-baseline interferometry

Daniel Bonneau, Florentin Millour, Anthony Meilland

▶ **To cite this version:**

Daniel Bonneau, Florentin Millour, Anthony Meilland. Observation of double star by long-baseline interferometry. F. Millour, A. Chiavassa, L. Bigot, O. Chesneau, A. Meilland & P. Stee. What can the highest angular resolution bring to stellar astrophysics?, 69-70, EDP sciences, 2015, EAS publication series, 978-2-7598-1833-4. 10.1051/eas/1569020 . hal-01221306

HAL Id: hal-01221306
https://hal.science/hal-01221306

Submitted on 27 Oct 2015

HAL is a multi-disciplinary open access archive for the deposit and dissemination of scientific research documents, whether they are published or not. The documents may come from teaching and research institutions in France or abroad, or from public or private research centers.

L'archive ouverte pluridisciplinaire **HAL**, est destinée au dépôt et à la diffusion de documents scientifiques de niveau recherche, publiés ou non, émanant des établissements d'enseignement et de recherche français ou étrangers, des laboratoires publics ou privés.

What can the highest angular resolution bring to stellar astrophysics?
Editors : F. Millour, A. Chiavassa, L. Bigot, O. Chesneau, A. Meilland & P. Stee
EAS Publications Series, Vol. 69-70, P.335-371, 2015

OBSERVATION OF DOUBLE STAR BY LONG BASELINE INTERFEROMETRY

D. Bonneau, F. Millour and A. Meilland[1]

Abstract. This paper serves as a reference on how to estimate the parameters of binary stars and how to combine multiple techniques, namely astrometry, interferometry and radial velocities.

1 Why binary stars matter?

The concept of physic stellar couples was imposed by astrometric observations of visual binaries in the XIXth century and the spectroscopic and photometric binaries in the early XXth century (Heintz, 1978). It quickly became apparent that the most interesting visual double stars were the one with a fast orbital motion (throughout an astronomer's life ...) so that with a small angular separation between the components whose astrometric measurement required high angular resolution (i.e. less than 1 arcsecond). It was found that the star formation process leads to extremely frequent stellar multiplicity with about two thirds of the stars belonging to a multiple system (Duchêne & Kraus, 2013). It was also found that the components of double stars could belong to all spectral types (related to temperatures and stellar masses) and that the physical separation of the components could vary considerably between wide binaries with separations large compared to the size of the stars (usually seen as visual binary or long period spectroscopic binary) and close binaries (observed as spectroscopic and photometric binaries) with separations which can be of the same order of magnitude as the size of the stars (Guinan et al., 2007). In this case, phenomena occur relating to the interaction between the components (mass transfer, circumstellar or circumbinary accretion disks, jets...).

When modeling stars, astrophysicists make very often the assumption that they were born, evolve and will die as a single star. This assumption, probably acceptable for wide binaries, is thrown into doubt more and more often for many types of stars and is no longer usable for close binaries. Indeed, for close binaries, the interactions that occur between components affect their evolutions no more similar to those of single stars. For example,

[1] Laboratoire Lagrange, UMR7293, Université de Nice Sophia-Antipolis, CNRS, Observatoire de la Côte d'Azur, Bd. de l'Observatoire, 06304 Nice, France
e-mail: fmillour@oca.eu

© EDP Sciences 2015
DOI: 10.1051/eas/1569020

very massive stars in the main sequence (O-type stars) were thought to be single a decade ago, but thanks to recent works of Sana et al. (2012), it has been demonstrated that almost all O stars are multiple. At the same time, recent developments in evolutionary models of stars allow one to consider the presence of a companion star (see for example (Siess et al., 2013)) and indeed it changes significantly the evolutionary tracks of stars.

The input of high angular resolution observations is fundamental to the study of the morphology of binary systems in addition to data provided by the spectroscopic and photometric observations. That is why the observation of double stars has become one of the main fields of application of interferometric techniques developed for high angular resolution astronomical observations. For about forty years, visual double stars and some spectroscopic binaries are accurately measured by speckle interferometry (Hartkopf et al., 2001), but in the last twenty years, the measurement and morphological study of the closer systems became possible by long baseline interferometry (see for example McAlister (2007) and Davis (2007)). However we do not forget that, to be fully usable, interferometric observations should be combined with spectroscopic, photometric, astrometric (Hipparcos, Gaia) observations, and the use of physical models of objects adapted to provide interferometric observable predictions (i.e. amplitude and phase of the fringe visibility).

Thus, the interferometric observations of double stars contribute

- To the determination of the fundamental stellar parameters (masses, radii);
- To the study of stellar evolution, from the initial phases (star formation, Initial Mass Function) at the end of life of the stars.

2 The Study of binary stars to determine stellar fundamental parameters

Validation of knowledge in the field of stellar physics relies heavily on our ability to confront the physical parameters (such as temperature, mass, and radius) predicted by the model and obtained from observations. We will see in this section that the determination of these parameters is possible by combining the interferometric observations with spectroscopic, astrometric, and photometric observations, depending on the class of the observed binary.

2.1 Components of a double line spectroscopic binary resolved as a visual binary

For a double line spectroscopic binary (SB2), the radial velocity measurements provide the spectroscopic orbits of the two components around the center of mass of the binary system. The case of a SB2 binary resolved as a visual double star whose stellar discs are resolved by interferometry is most favorable for the determination of stellar fundamental parameters (see Figure 1).

It should first be noted that the distance of the system can be determined by combining the spectroscopic and apparent orbits. The accuracy of the orbital parallax depends more

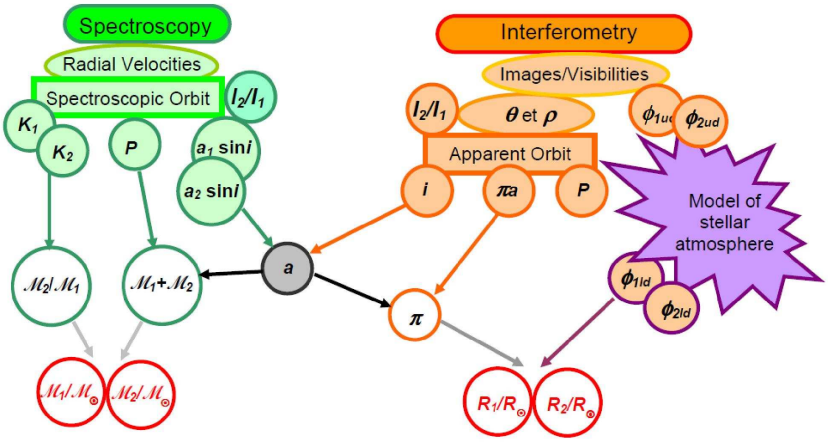

Fig. 1. Determination of Masses and Radii for a resolved double line spectroscopic binary

on the quality of spectroscopic and interferometric measurements than of the distance of the system. Then, the values of the stellar masses are then directly obtained by combining the visible and spectroscopic orbits.

Moreover, the use of a model of stellar atmosphere is necessary to obtain the value limb-darkened angular diameter ϕ_{ld} from the uniform disc angular diameter ϕ_{ud} given by interferometric measurements.

The value of the intensity ratio of the two components I_2/I_1 can be derived from spectroscopic analysis as well as the visibility measurements (see 4.1). Further spectrophotometric data are needed to estimate the effective temperature and the luminosity of each system components.

2.2 Components of a single line spectroscopic binary resolved as a visual binary

For a single line spectroscopic binary (SB1), the radial velocity measurements provide only the spectroscopic orbit of the brightest component.

Interferometric observations resolve the system as a visual binary and allow computing the apparent orbit and giving an estimate the intensity ratio of the components (see Figure 2).

Generally, only the angular diameter of the primary component can be estimated from the interferometric visibility analysis. The use of a model of stellar atmosphere is necessary to obtain the value limb-darkened angular diameter ϕ_{ld} from the uniform disc angular diameter ϕ_{ud}. The determination of the stellar masses and radii requires knowledge of the distance of the system determined from astrometric observations. Further spectrophotometric data are needed to estimate the effective temperature and the luminosity of each system component.

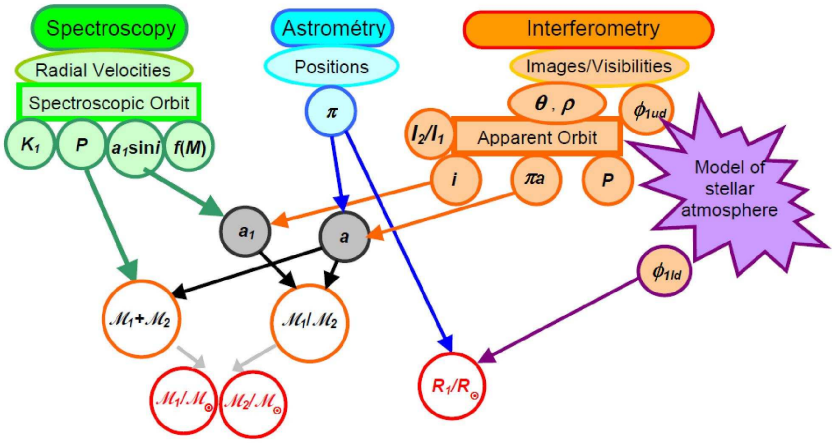

Fig. 2. Determination of Masses and Radii for a resolved single line spectroscopic binary

3 The orbit of a binary star

There is an extensive literature on the subject of double stars and many websites are devoted to this topic and much information is available on the Web site of the "*Double Star Library*" [1]. We only recall some basic and the contribution of interferometric observations to the measurement of double stars.

The measure of a binary star consists in recording the relative positions of the components in a tangent plane to the celestial sphere (the sky plane) at a given epoch t. As shown in Figure 3 the coordinates of the B component relative to the position of the A component are:

$$X = \rho\, cos\theta = \Delta\alpha\, cos\delta, \quad Y = \rho\, sin\theta = \Delta\delta. \tag{3.1}$$

With, the position angle θ (in degree) measured from the North (0°) to the East (90°) and the angular separation ρ (in arcsecond).

The main purpose of the double star observations is to obtain orbits whose knowledge is the key to determining the masses and even stellar distances, fundamental parameters of stellar astrophysical studies. The contribution of the interferometric observations in addition to spectroscopic and photometric observations is valuable for the astrophysical study of double stars.

The orbit of a double star reflects the motion of the stars under the influence of gravity and therefore obeys the Newton's and Kepler's laws.

Three types of orbits may be considered to describe the orbit of a double star (components A and B) bound by the gravitation:

[1] http://www.usno.navy.mil/USNO/astrometry/optical-IR-prod/wds/dsl

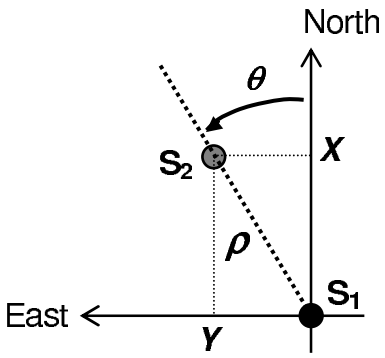

Fig. 3. Measure of a *visual double star*

- The (A/AB) and (B/AB) *absolute orbits* of A and B around the center of mass AB respectively. For resolved binaries, astrometric observations give then access to the (AB/A) and (AB/B) orbits projected on the sky plane and spectroscopic measurements of the radial velocity allow to determine the (AB/A) and (AB/B) orbits projected on the line of sight. In the case of a binary with large magnitude difference, the astrometric measurements capture the position of the photocenter F located between A and AB which determines the (F/AB) *astrometric orbit* with a semi-major axis aF and radial velocity measurements give only access to the (A/AB) orbits projected on the line of sight.

- The *relative orbit* (B/A) of B around A (Figure 4). The (B/A) orbit projected on the sky plane, known as the *apparent orbit*, can be derived from measurements of the relative position of the components obtained with astrometric imaging or interferometric observations.

It should be noted that, for a given projected orbit on the sky plane, there is two possible true orbits, which are symmetric with respect to the sky plane.

3.1 Classical orbital parameters

The spatial motion of the binary components is described using the reference frame (A, x, y, z) centred on the A component with two axes in the plane tangent to the celestial sphere *plane of the sky*: Ax axis points towards the North (position angle = 0°), Ay axis points towards the East (position angle = 90°). The Az axis is along the line of sight, pointing in the direction of increasing radial velocities (positive radial velocity).

This reference frame is thus retrograde: viewed from the positive side of the Az-axis, a rotation of the Ax-axis onto the Ay-axis is carried out clockwise. The relative (B/A) orbit is described by means of seven *classical orbital elements*.

Four so-called *dynamic elements* specifying the properties of the Keplerian motion in the true orbit:

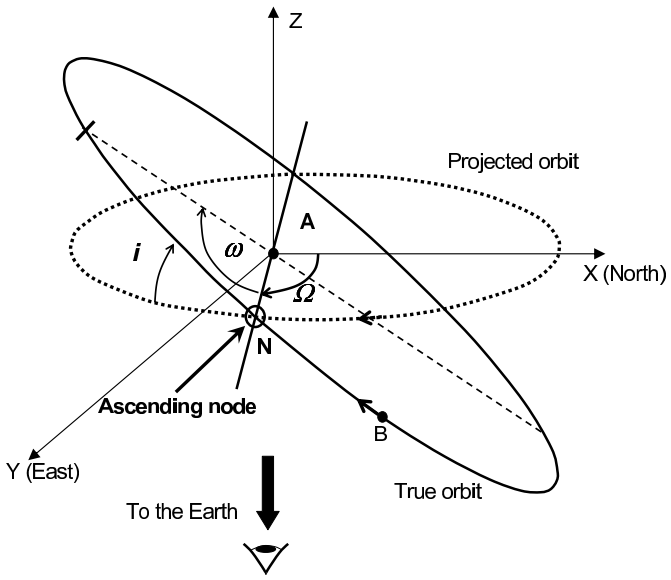

Fig. 4. The true and the projected (B/A) orbits of a *visual double star* and its geometrical elements

- T, the epoch of passage through periastron expressed in Julian days or in Besselian years [2].
- P, the revolution period (in day or in year)
- a, the true semi-major axis (in km or au[3]) or $a'' = \varpi a$, the apparent semi-major axis (in arcsecond)
- e, the eccentricity

Three so-called *geometric elements* which define the orientation of the orbits (see Fig. 4) are:

- Ω, is the position angle of the line of intersection between the true orbital plane and the plane of the sky. There are two nodes whose position angles differ by 180°but by convention, Ω is the position angle of the *ascending node* (where the orbital motion is directed away from the Sun). If radial-velocity measurements are not available to identify the *ascending node*, a temporary value ranging between 0°and 180° is adopted following a convention proposed by (Finsen, 1934).

[2]the "Besselian epoch" can be calculated by $B = 1900.0 + (Julian\ date - 2415020.31352)/365.242198781$

[3]astronomical unit is written "au", instead of "AU", since the 2012 IAU resolution B2 "on the re-definition of the astronomical unit of length"

- i, the inclination, is the angle between the planes of the projected orbit and of the true orbit, taken at the ascending node. The motion is prograde if $0° < i < 90°$ and retrograde if $90° < i < 180°$.
- ω, is the argument of the periastron in the true orbit plane, measured in the direction of the orbital motion from the *ascending node* with a value ranging from 0° to 360°.

3.2 Total mass of the system

For a binary system whose relative (B / A) orbit and the distance is known, the total mass can be calculated by application of Kepler's third law.

$$M = M_A + M_B = \frac{a^3}{\varpi^3\ P^2}, \tag{3.2}$$

with, $\varpi = 1/d$, the parallax (in arcsecond) and d the distance (in parsec) of the double star, M the total mass of the system in solar mass $M_\odot$, a the semi-major axis (in au), and P the orbital period (in year).

The relative error on the total mass can be estimate with:

$$\frac{\Delta M}{M} \approx 3\ \frac{\Delta a}{a} + 2\ \frac{\Delta P}{P} + 3\ \frac{\Delta \varpi}{\varpi}. \tag{3.3}$$

It should be noted that for a well determined orbit, errors on parameters a and P are independent and the error on the mass of the system is dominated by the parallax error.

3.3 The true orbit

The true (B/A) orbit is the Keplerian elliptical orbit of the B around A.

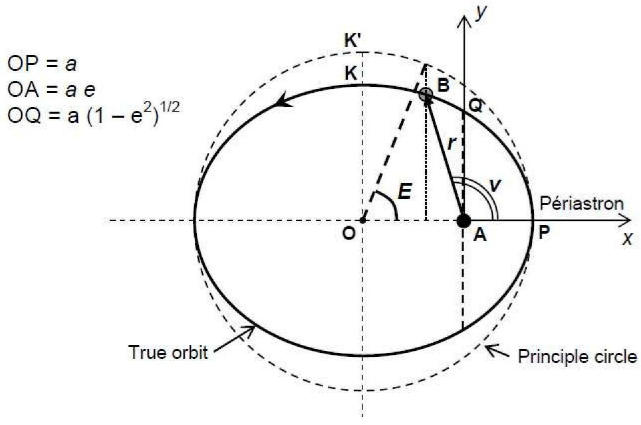

Fig. 5. The true (B/A) relative orbit

The position of the B component (Figure 5) is given by the Cartesian coordinates x, y:

$$x = cosE - e = \frac{r}{a}\, cosv, \quad y = \sqrt{(1-e^2)}\, sinE = \frac{r}{a}\, sinv, \tag{3.4}$$

with r the radius vector such as,

$$r = \frac{a\,(1-e^2)}{(1+e\,cosv)}. \tag{3.5}$$

Following the second Kepler's law, the radius vector sweeps out equal areas in equal time differences. The area constant C is equal to the area of the ellipse divided by the period:

$$C = \frac{1}{2}\, r^2\, \frac{dv}{dt} = \frac{\pi\, a^2}{P}\, \sqrt{(1-e^2)}. \tag{3.6}$$

In the plane of the true orbit, the motion is described by Kepler's equation:

$$E - e\, sinE = \frac{2\,\pi\,(t-T)}{P} = M, \tag{3.7}$$

with t the observation date, E the eccentric anomaly, M the mean anomaly, and v the true anomaly so that:

$$tan\frac{v}{2} = \sqrt{\frac{1+e}{1-e}}\, tan\frac{E}{2}. \tag{3.8}$$

3.4 The apparent orbit

The apparent orbit is the projection of the true relative (B/A) orbit on the sky plane (see Figure 6). The center O of the apparent ellipse is the center of the true orbit so that, the line joining O and A is the projection of the semi-major axis of the true (B/A) orbit and the orbital eccentricity is given by $e = OA/OP$. The line O, K' parallel to the tangent at the apparent orbit at periastron P is the projection of the diameter of the principal circle of the true (B/A) orbit. The positions X, Y of the B component on the sky plane can be computed from the true orbital positions x, y using:

$$X = A\, x + F\, y, \quad Y = B\, x + G\, y. \tag{3.9}$$

The coefficients A, B, F, and G are known to be the *Thiele-Innes elements* related to the classical orbital elements by:

$$A = a\, (\cos\omega\, \cos\Omega - sin\omega\, sin\Omega\, \cos i)\,, \tag{3.10}$$

$$B = a\, (\cos\omega\, sin\Omega + sin\omega\, \cos\Omega\, \cos i)\,, \tag{3.11}$$

$$C = a\, (-sin\omega\, \cos\Omega - \cos\omega\, sin\Omega\, \cos i)\,, \tag{3.12}$$

$$G = a\, (-sin\omega\, sin\Omega + \cos\omega\, \cos\Omega\, \cos i)\,. \tag{3.13}$$

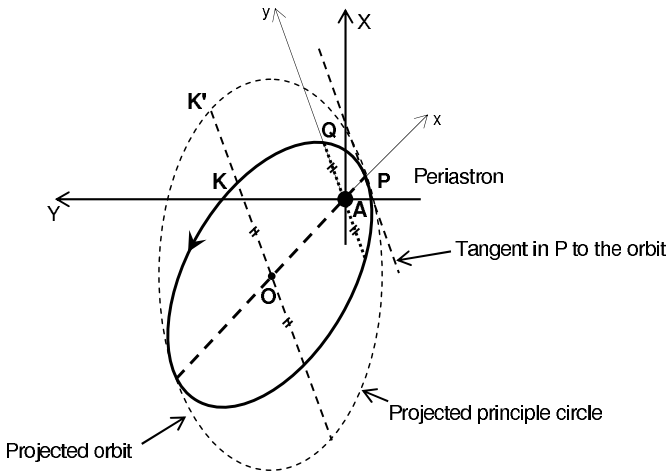

Fig. 6. The apparent (B/A) relative orbit also called the *visual orbit*

The accumulation of measurements of the relative positions of the components with respect to time allows to plot the apparent (B/A) orbit. From there, several methods are used to obtain values of the orbital elements. Determining an orbit is a nonlinear problem whose solution is generally obtained in two steps: computing an initial orbit, and improvement thereof by minimizing $(O - C)$ residual using a least-square minimization. The geometric method of adjusting the elliptical apparent orbit on the observed positions and determining the orbital elements using the Thiele-Innes elements, provides a first estimate of the orbital elements (see for example Heintz (1978)). One can also obtain the initial orbit using methods of automatic calculations to obtain the values of the orbital elements that give minimum residual between the observed and calculated positions (see for example Pourbaix, 1994).

3.5 Ephemeris formulae

For a given observing date t, the angular separation ρ and the position angle θ of a double star whose orbital elements are known can be calculated using the ephemeris formulae. The eccentric anomaly E is obtained by solving the Kepler's equation (Equation 3.7), the true anomaly v and the radius vector r given by equations 3.8 and 3.5 respectively. Then, ρ and θ are computed using formulae:

$$tan(\theta - \Omega) = tan(v + \omega)\ \cos i, \tag{3.14}$$

$$\rho = r\,\frac{\cos(v + \omega)}{\cos(\theta - \Omega)}. \tag{3.15}$$

The knowledge of some particular positions can be interesting within the framework of the preparation of interferometric observations to resolve a spectroscopic binary:

Periastron: $v = 0°$,

$$r_P = a\,(1-e), \quad tan(\theta_P - \Omega) = tan\omega\ \cos i, \quad \rho_P = a\,(1-e)\,\frac{\cos\omega}{\cos(\theta_P - \Omega)}. \tag{3.16}$$

Apoastron: $v = 180°$,

$$r_{P'} = a\,(1+e), \quad \theta_{P'} = \theta_P + 180°, \quad \rho_{P'} = -a\,(1+e)\,\frac{\cos\omega}{\cos(\theta_{P'} - \Omega)}. \tag{3.17}$$

Ascending node: $v = 360° - \omega$,

$$r_\Omega = a\,\frac{(1-e^2)}{(1+e\ \cos\omega)}, \quad (\theta_\Omega - \Omega) = 0°, \quad \rho_\Omega = a\,\frac{(1-e^2)}{(1+e\ \cos\omega)}. \tag{3.18}$$

descending node: $v = 180° - \omega$,

$$r_{\Omega'} = a\,\frac{(1-e^2)}{(1-e\ \cos\omega)}, \quad (\theta_{\Omega'} - \Omega) = 180°, \quad \rho_{\Omega'} = -a\,\frac{(1-e^2)}{(1-e\ \cos\omega)}. \tag{3.19}$$

It should be noted that the relative position of the component at the time of the passage to the node gives the orientation of the line of Nodes in the sky plane and does not depend on the orbital inclination.

3.6 The spectroscopic orbits

If V_{rA}, V_{rB} are the heliocentric radial velocities of components A and B respectively and V_{rAB} the radial velocity of the center of mass AB of the binary and denoting $V_{AB/A}$ and $V_{AB/B}$ the radial components of the orbital velocity of A and B around the center of mass, then:

$$V_{rA} = V_{AB/A} + V_{rAB}, \quad V_{rB} = V_{AB/B} + V_{rAB}, \tag{3.20}$$

with the radial velocity V_{rAB} of the center of mass or systemic velocity V_{sys}:

$$V_{sys} = V_{rAB} = \frac{1}{P}\int_0^P V_R(t)dt, \tag{3.21}$$

where V_R is the stellar radial velocity obtained from the measurement of the spectral lines:

$$V_R = V_{sys} + \frac{dz}{dt}. \tag{3.22}$$

With z the radius vector r projected onto the line of sight:

$$z = r\ sin(v+\omega)\ sini. \tag{3.23}$$

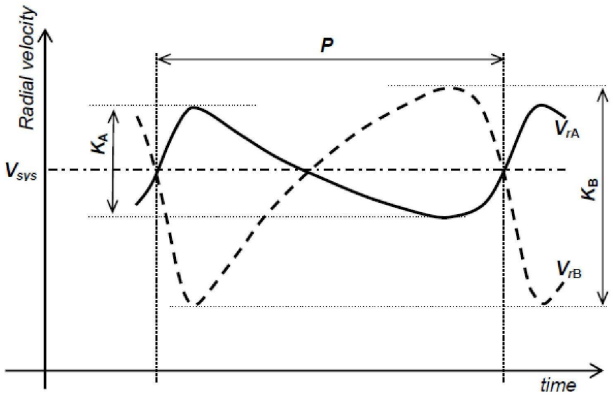

Fig. 7. Radial velocity curves for the components of a spectroscopic binary

The orbital radial velocity of each component relates to the classical orbital elements by:

$$\frac{dz}{dt} = \frac{2\,\pi}{P}\,\frac{a\ sini}{\sqrt{1-e^2}}\,[\cos(v+\omega)+e\ \cos\omega]\,, \tag{3.24}$$

where v is the true anomaly, P the orbital period, a are the semi-major axis a_A or a_B, and ω the argument of the periastron ω_A or ω_B of the (A/AB) and (B/AB) orbits respectively. Defining:

$$K = \frac{2\,\pi}{P}\,\frac{a\ sini}{\sqrt{1-e^2}}. \tag{3.25}$$

The maximum and minimum radial velocities are:

$$V_{max} = V_{sys} + K(1+e\ \cos\omega), \quad V_{min} = V_{sys} + K(e\ \cos\omega - 1). \tag{3.26}$$

The semi-amplitude of variation of the radial velocity being K and its median value V_{med} can be estimated using:

$$K = \frac{V_{max} - V_{min}}{2}, \quad V_{med} = \frac{V_{max} + V_{min}}{2} = V_{sys} + K\,e\ \cos\omega. \tag{3.27}$$

At the date of passage to the periastron T:

$$V(T) + V(T + \frac{P}{2}) = 2\ V_{med}, \tag{3.28}$$

then the radial velocities at the time of passage at periastron and the apoastron are:

$$V_{per} = V_{med} + K\ \cos\omega, \quad V_{apo} = V_{med} - K\ \cos\omega, \tag{3.29}$$

from which it follows the determination of ω the argument of the periastron using:

$$K\ \cos\omega = \frac{V_{per} - V_{apo}}{2}. \tag{3.30}$$

For double line spectroscopic binaries (SB2), the measurements of $V_{A/AB}$ and $V_{B/AB}$ are possible; for single-lined spectroscopic binaries (SB1), only $V_{A/AB}$ measurements are possible.

For visual binaries, the relative radial velocity between the components, $V_r = V_{rB} - V_{rA}$, can be calculated from the orbital elements of the (B/A) orbit using:

$$V_r = K\ [\cos(v+\omega) + e\ \cos\omega]\,, \tag{3.31}$$

with,

$$K(km/s) = 29,76\ \frac{a\ sini}{P\ \sqrt{1-e^2}}, \tag{3.32}$$

for P in year, and

$$K(km/s) = 10870\ \frac{a\ sini}{P\ \sqrt{1-e^2}}, \tag{3.33}$$

for P in day.

For an astrometric binary orbit, the radial velocity of the photocenter V_{rF} can be computed with the same formula where the semi-major axis a_F and the argument of the periastron ω_F of the photocenter orbit have been inserted instead. It is easy to show that $\omega_A = \omega_F = \omega_B + 180°$.

The variation of V_r and V_{rB} are the same and are opposite to that of V_{rA}. By definition, the maxima of the V_{rA} and V_{rB} curves occurs at the passage of the ascending node in the true orbits (A/AB) and (B/AB) respectively, whereas the maximum of the V_r curve corresponds to the passage at the ascending node in the relative orbit (B/A).

3.6.1 Double line spectroscopic binary

The lines of the two components are visible in the composite spectrum. The radial velocities curves of the two components can be then determined and allow calculating the (A/AB) and (B/AB) orbits around the center of mass:

$$a_A\ sini = \frac{P}{2\ \varpi} K_A\ \sqrt{1-e^2}, \quad a_B\ sini = \frac{P}{2\ \varpi} K_B\ \sqrt{1-e^2}. \tag{3.34}$$

Mass ratio and lower limit of the stellar masses

The semi-major axis of the absolute orbits being function of the stellar masses,

$$a_A = a\ \frac{M_B}{M_A + M_B}, \quad a_B = a\ \frac{M_A}{M_A + M_B}, \tag{3.35}$$

with $a = a_A + a_B$ the semi-major axis of the relative (B/A) orbit.

The **mass ratio** $\frac{M_B}{M_A}$ is equal to the ratio of the amplitudes of the radial velocity curves:

$$\frac{M_B}{M_A} = \frac{a_A}{a_B} = \frac{K_A}{K_B}. \tag{3.36}$$

The determination of the spectroscopic orbit provides an estimate of the **lower limit of the stellar masses** of the system.

With P in days, K in km / s, and M in solar mass it comes:

$$\begin{aligned} M_B\ sin^3 i &= 1,036\ 10^{-7}\ K_A\ (K_A + K_B)^2\ P\ \left(1 - e^2\right)^{3/2}, \\ M_A\ sin^3 i &= 1,036\ 10^{-7}\ K_B\,(K_A + K_B)^2\ P\ \left(1 - e^2\right)^{3/2}, \end{aligned} \tag{3.37}$$

and then,

$$(M_A + M_B)\ sin^3 i = \frac{P}{2\,\pi\,G}\ \left(1 - e^2\right)^{3/2}\ \ (K_A + K_B)^3\,. \tag{3.38}$$

Contribution of interferometric observations

If a SB2 spectroscopic binary is resolved by interferometric observations, determination of the orbital elements of the (B/A) orbit provides the value of the angular semi-major axis a'' and the inclination i. An estimation of the distance of the system can be obtain from the ratio $a/a'' = d = 1/\varpi_{orb}$, with ϖ_{orb} the *orbital parallax*. The combination of the mass ratio M_B/M_A from the spectroscopic orbits and the total masse $M_A + M_B$ from visual (B/A) orbit is then used to calculate the values of the stellar masses M_A and M_B of each component.

3.6.2 Single line spectroscopic binary

Only the spectral lines of one of the component are recorded, this is usually due to a large magnitude difference in between the two components. So, only the radial velocity curve of the brightest component can be used to calculate the (A/AB) orbit around the center of mass, giving:

$$a_A\ sini = \frac{P}{2\,\varpi}\ K_A\ \sqrt{1 - e^2}. \tag{3.39}$$

Mass Function

For SB1 binary, only a combination of the stellar masses, called the *Mass Function* can be determined from the spectroscopic orbit:

$$f(M) = (M_A + M_B)\ \left(\frac{M_B}{M_A + M_B}\right)^3\ sin^3 i = \frac{P}{2\,\pi\,G}\ \left(1 - e^2\right)^{3/2}\ K_A^3. \tag{3.40}$$

With P in days, K in km/s, and M in solar masses it comes:

$$a_A\ sini = 1375\ K_A\ P\ \sqrt{1 - e^2} \qquad f(M) = 1.036\ 10^{-7}\ P\ \left(1 - e^2\right)^{3/2}\ K_A^3. \tag{3.41}$$

Contribution of interferometric observations

If a SB1 spectroscopic binary is resolved by interferometric observations, determination of the (B/A) orbit provides the value of the angular semi-major axis a'' and the inclination i. If the distance of the system is known (by the trigonometric parallax for example) , the combination of parameters of spectroscopic and visual orbits is then used to calculate the values of the stellar masses. The linear semi-major axis (in au) $a = a'' / \varpi_{trig}$ of the (B/A) orbit and the total mass of the system ($M_A + M_B$) being known, the semmajor axis of the (A/AB) orbit a_A can be calculated from the a_A *sini* of the spectroscopic orbit allowing estimation of the mass ratio $M_B/(MA + MB) = a_A/a$ and the stellar masses M_B and M_A.

It should be noted that in the case of a SB1 or SB2 spectroscopic binary resolved as visual binary, the orbital parameter setting can be obtained by combining astrometric and radial velocity measurements (see for example Pourbaix (1998)).

4 Interferometric observation of double stars

The studies of the morphology of double stars still need to use observations at high angular resolution. Long baseline interferometry differs from other astrometric observations of double stars by a large gain in angular resolution. While CCD imaging achieved a resolution of about $0.25''$ for observing visual binaries, and speckle interferometry reaches $0.05''$ resolving as *visual binaries* some spectroscopic binaries, the long baseline interferometry reaches resolution of the order of $0.001''$ and therefore it allows to resolve many spectroscopic binaries and even some photometric binaries.

This explains why the double stars were among the earliest targets for the interferometric observations. One can find all the interferometric measurements of binary stars in the "*Fourth Catalog of Interferometric Measurements of Binary Stars*" [4].

For a long baseline interferometric observation of a double star, two quantities must be taken into account (Figure 8), the relative position of the two components projected in the sky plane, characterized *star vector* and the projection on the sky of the interferometric baseline, characterized by the *baseline vector*.

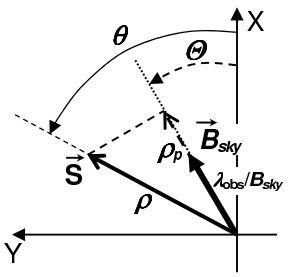

Fig. 8. *Star vector* and *baseline vector* on the skyplane

These vectors are described using the reference frame (A, x, y, z) centered on the A

[4] http://ad.usno.navy.mil/wds/int4.html

component with two axes in the plane tangent to the sky plane: Ax points towards the North (position angle 0°), Ay points towards the East (position angle 90°).

The *star vector* is characterized by its length equal to the angular separation of the components and its direction is given by position angle of the two stars (see Figure 8),

$$\vec{S} = (S_X, S_Y) = (\rho\ \cos\theta, \rho\ sin\theta). \tag{4.1}$$

The double star is also characterized by the ratio of the intensities I_2/I_1 (or the difference of magnitudes $\Delta\, m = m_2 - m_1$) of these components:

$$R = I_2/I_1 = 10^{-0.4\Delta m}. \tag{4.2}$$

The *baseline vector* (see Figure 8) is characterized by the length B_{sky}/λ and direction Θ of the projection on the sky of the interferometric *ground baseline*. The *ground baseline vector* will be assumed here horizontal with a length and direction that are defined in a geodetic coordinate system [5].

$$\vec{B_{gro}} = (B_N, B_E), \tag{4.3}$$

with B_N and B_E the projections toward North and East of the *ground baseline*.

$$\vec{B_{sky}} = (B_X, B_Y), \tag{4.4}$$

with:

$$B_X = \cos H\ sin\delta\ sinL - \cos\delta\ \cos L, \quad B_Y = sinH\ sinL, \tag{4.5}$$

and the polar coordinates $B_{sky} = (B_X^2 + B_Y^2)^{1/2}$ and $tan\Theta = B_Y/B_X$.

The *sky baseline vector* depends on the latitude L of the observatory as well as the position of the target star in the sky defined by its equatorial coordinates (right ascension α and declination δ) and the hour angle of observation ($H = ST - \alpha$). Thus, with a fixed *ground baseline*, the *sky baseline vector* is constantly variable depending on the time of observation (i.e. the sidereal time ST).

A key parameter for interferometric observation of a double star is the projection of the *star vector* on the direction of the *baseline vector* (see Fig. 8), the length of which is:

$$\rho_p = \rho\ \cos(\theta - \Theta). \tag{4.6}$$

In the following we will see that the interferometric observation of a double star can be done in two ways:

- by recording the fringe visibility of a double source;
- by recording the fringes of each separated stellar components.

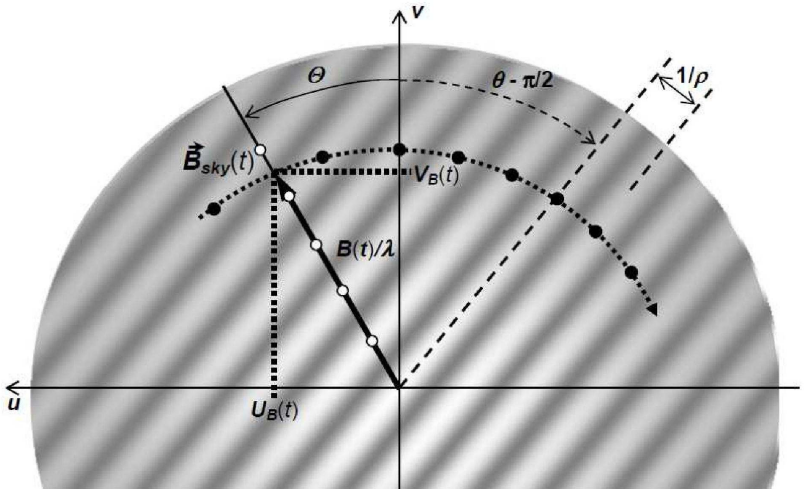

Fig. 9. Star fringe visibility and baseline vector on the uv plane

4.1 interferometer observing a double source

For the analysis of interferometric observations, it is common to consider vectors in Fourier space (u, v), i.e. the spatial frequency domain (see Fig. 9). In this space, an interferometer characterized by a *sky baseline vector* $\vec{B}_{sky}$ and observing at the wavelength λ must be regarded as a filter isolating the single *spatial frequency vector* $\vec{f}$:

$$\vec{f} = (f_u, f_v) = \frac{\vec{B}_{sky}}{\lambda}, \tag{4.7}$$

with the coordinates,

$$\begin{aligned} f_u &= \frac{1}{\lambda}[-B_N \; sinL \; sinH - B_E \; \cos H], \\ f_v &= \frac{1}{\lambda}[B_N \; \cos L \; \cos\delta + sinL \; sin\delta \; \cos H + B_E \; sin\delta \; sinH]. \end{aligned} \tag{4.8}$$

In this space, a double star will be represented by a *corrugated sheet* characterized by:

- the period of the fringes $\Lambda = 1/\rho$;
- the orientation of the fringes given by the position angle θ of the binary;
- the amplitude of modulation of the fringes, function of the intensity ratio of the components and their angular diameters, is given by the function of visibility $V(f)$

[5]The World Geodetic System (WGS) is a standard for use in cartography, geodesy, and navigation.

of the source i.e. the Fourier transform of the light intensity distribution on the source:

$$V(f) = \frac{1}{1+R}\sqrt{[V_1(f)^2 + R^2\ V_2(f)^2 + 2\ R\ V_1(f)\ V_2(f)\ \cos\psi]^{1/2}}, \tag{4.9}$$

with $\psi(f) = 2\,\pi\,\rho_p\ f$, and the value of the visibility oscillates between V_{max} and V_{min} values:

$$V_{max} = \frac{V_1(f) + R\ V_2(f)}{1+R}, \quad V_{min} = \frac{V_1(f) - R\ V_2(f)}{1+R}. \tag{4.10}$$

$V(f)$ is the amplitude of the complex visibility of the source:

$$\tilde{V}(f) = \frac{V_1(f)}{1+R}\exp i\frac{R\,\psi}{1+R} + \frac{V_2(f)}{1+R}\exp -i\frac{\psi}{1+R} = V(f)\ \exp i\Phi(f), \tag{4.11}$$

$V_1(f)$ and $V_2(f)$ are the visibility functions of the stellar disk of each component. The phase Φ of the complex visibility is calculated relatively to the position of the photometric barycenter (photocenter) of the intensity distribution on the source, with:

$$tan\Phi(f) = \frac{V_1(f)\ sin\frac{R\ \Psi(f)}{1+R} - R\ V_2(f)\ sin\frac{\Psi(f)}{1+R}}{V_1(f)\cos\frac{R\Psi(f)}{1+R} - R\ V_2(f)\ \cos\frac{\Psi(f)}{1+R}}. \tag{4.12}$$

Observational procedures

As seen before, the earth rotation produces a rotation of the projected *baseline vector* on the sky and then a change of the spatial frequency measured by the interferometer as function of time. At a given time, the length of the baseline vector is inversely proportional to the wavelength of observation. These findings are the basis of the two observational procedures that can be used for the measurement of the fringe visibility of a double star.

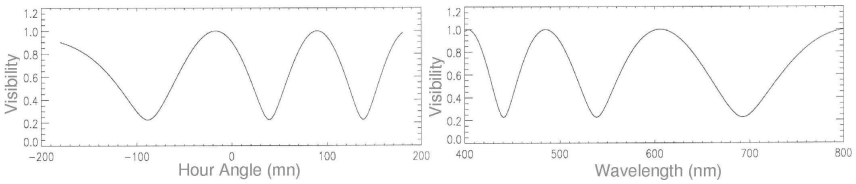

Fig. 10. Variation of the amplitude of the visibility function for a double star. Up: variation of the fringe visibility as function of time (Hour Angle) at $\lambda = 600\ nm$. Down: variation of the fringe visibility as function of the wavelength at $HA = 0$.
These curves was computed for a double star at $\delta = 43.75°$ with $\rho = 20\ mas$, $\theta = 45°$, $\Delta\ m = 0.5\ mag$, angular diameter of the components $\phi_{ud} = 0.1\ mas$ and for a North-South $25m$ baseline interferometer at $L = 43.75°$.

A - Variation of visibility over time.

For given wavelength and ground baseline, the earth's rotation produces a variation in the orientation of the baseline vector on a resulting change with time of the angular separation projected on the *baseline vector*.

As shown in left side of Figure 10, the variation of the amplitude of the visibility as function of time presents a series of maxima and minima. From equation 4.9 it comes that:

- *Maximum visibility* occurs for Hour Angles H_{max} so that $\rho_p = k\ \lambda/B_{sky}$
- *Minimum visibility* occurs for Hour Angles H_{min} so that $\rho_p = (k + \frac{1}{2})\ \lambda/B_{sky}$

with k (integer) the interference order, the wavelength λ, B_{sky} the length of the projected baseline, and ρ_p the projected angular separation.

This method can be implemented for the interference fringes obtained in filtered light was used by the majority of interferometers since the late 1980s, including Mark III (1985-1998), SUSI (since 1991) IOTA (1993-2006), PTI (1995-2008).

The Figure 11 shows early example of this type of procedure for the observations of the double line spectroscopic binary α Equulei with the MarkIII interferometer (Armstrong et al., 1992).

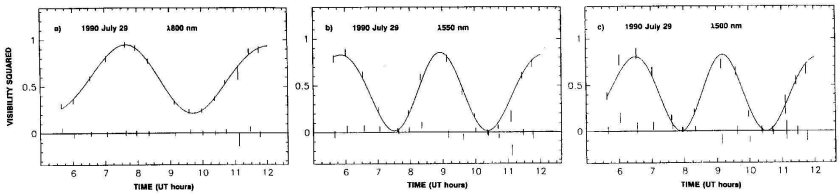

Fig. 11. Example of observations of α Equulei with the MarkIII interferometer for the night 1990 july 29. Plot of the V^2 as function of time at $\lambda = 800,550\ nm$ for a baseline length projected at Transit ($H = 0$) and $B_{sky} = 23,7\ m$. The error bars on data are $\pm 1\ \sigma$. The line showns the visibility computed from the best model adjustment giving $\rho = 11,48\ mas$ and $\theta = 62,4$ deg. (From Figure 1 in Armstrong et al. (1992))

.

The visibility measurements at wavelengths 800, 550, 500 and 450 nm, made during 29 nights in 1989 and 1990, were used to determine the relative positions of the components (ρ, θ) for each of those nights and the values of the magnitude differences $\Delta\ m\ (\lambda)$ in the observed spectral bands. For the first time, the elements of the apparent orbit of α Equ were obtained by fitting the orbit on the observed positions (Fig.12). This orbit, combined with spectroscopic parameters of Rosvick & Scarfe (1991) allows to determine the masses and distance of the system. A comparison with the stellar evolution models was then made using the stellar masses, differences in magnitudes, and absolute magnitudes of the components (spectral type G5 III and A5 V) determined from interferometric observations.

B - Variation of the visibility as function of the wavelength.

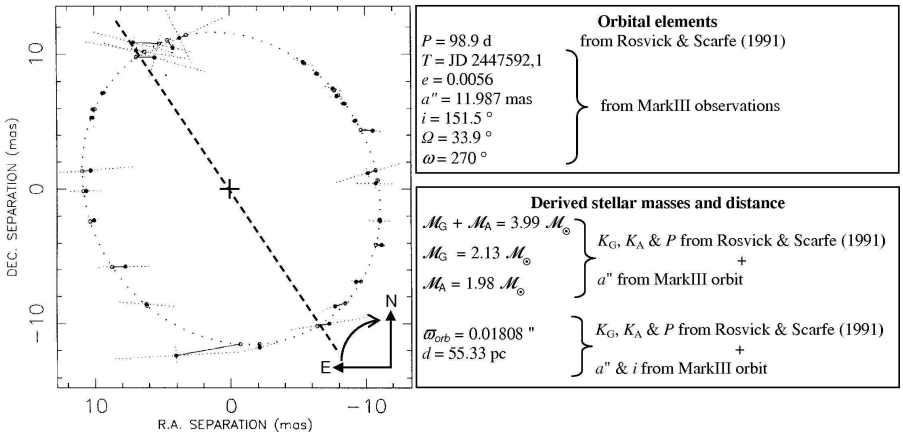

Fig. 12. Right: Apparent orbit of α Equulei determined from MarkIII interferometric observations, from Figure 2 in Armstrong et al. (1992). Left: Orbital elements of the relative apparent orbit, stellar masses, and distance of α Equ derived from MarkIII observations (Armstrong et al., 1992).

For fixed length of the ground baseline and a given hour angle, the observed spatial frequency depends on the wavelength. For a given angular separation projected on the *baseline vector*, this results in a variation of the value of fringe visibility as a function of wavelength and the amplitude of the visibility presents a series of maxima and minima over the spectrum as it is shown in right side of Figure 10. From equation 4.9 it comes that:

- *Maximum visibility* occur for the wavelengths $\lambda = 4.848\ B_{sky}\ \rho_p/k$;
- *Minimum visibility* occur for the wavelengths $\lambda = 4.848\ B_{sky}\ \rho_p/(k + 1/2)$;

with k (integer) the interference order, the wavelength λ, B_{sky} the length of the projected baseline, and ρ_p the projected angular separation.

To be used, this method requires that the fringes are recorded by dispersing the light from the star. It was implemented for the first time on the interferometer I2T the Observatory Calern (France) in the late 1970's and now can be used with instruments such as AMBER on the VLTI in the IR or VEGA on CHARA in the visible.

On a basic way, these two procedures allow to determine the values of the projected angular separation ρ_p at different times of observation. Knowing the value of the position angle Θ of the baseline vector projected on the sky as function of the time, it is possible to deduce the value of the angular separation ρ and position angle θ of the double star.

A more complete determination of the parameters of the double star (ρ, θ, R, and also ϕ_1 and ϕ_2) can be obtained by adjusting on the measured amplitude and phase of the visibility a computed visibility curve using a model of the double star. This adjustment can be done using LITpro the model fitting software developed by the "*Centre Jean-Marie*

Mariotti" (JMMC) [6].

An illustration of this observation mode is given by the observations of the binary Be star δ Scorpii observed with the AMBER focal instrument of the VLTI (Meilland et al., 2011). δ Sco, resolved as a visual binary of high eccentric orbit by speckle interferometry since 1974, is also known as single lines spectroscopic binary (Miroshnichenko et al., 2001). Long baseline optical interferometric observations were first performed in the visible with the Sydney University Stellar Interferometer (SUSI) by measuring the visibility as function of time (Tango et al., 2009) and then with the Navy Precision Optical Interferometer (NPOI) from polychromatic visibility measurements (Tycner et al., 2011). As shown in the figure 13 the VLTI/AMBER interferometric observations were used to measure the visibility of the fringes dispersed in the near IR K-band around 2.2 μm. Using the software LITpro, the relative position of the components was obtained by fitting the observed visibility curves by a model four free parameters: the relative position of the components (X, Y), the flux ratio (F_1/F_{tot}), the diameter of the primary component (D_1), the secondary component assumed to be a point source. These new position measurements have been combined with all the published positions and radial velocity measurements to obtain the values of orbital parameters $(P, T_0, e, a", i, \Omega, \omega)$ of the relative orbit and the parameters (V_0, K_1) of the spectroscopic orbit of the primary component (Figure 14) and for details see Meilland et al. (2011).

.

4.2 Double star observed as two single stars

In this case, the double star can be described as two stars whose positions on the sky (α_1, δ_1) and (α_2, δ_2) corresponding to differences $\Delta\delta = \rho\cos\theta$ in declination and $\Delta\alpha = \rho sin\theta/\cos\delta_1$ in right ascension. The differential star vector $\vec{S}_{12}$ is characterized by the angular separation of the two stars ρ and the position angle θ with an angular separation projected on the baseline vector ρ_p.

As shown in Fig. 15, the projection of this differential star vector $\vec{S}_{12}$ on the sky baseline vector $\vec{B}_{sky}$ results in the formation of two fringe packets F_1 and F_2 associated with each component and separated by an optical path difference of $\Delta\delta_{opt}$.

For a north-south horizontal baseline, we can write (Kovalevsky, 1995):

$$\Delta\delta_{opt}(H) = B_{gro}[(\sin L\cos\delta_1\sin H)\Delta\alpha - (\sin L\sin\delta_1\cos H - \cos L\cos\delta_1)\Delta\delta], \quad (4.13)$$

with, $\Delta\alpha = \alpha_1 - \alpha_2$ and $\Delta\delta = \delta_1 - \delta_2$, L the latitude of the interferometer and H the Hour Angle of the observation. Once the fringes are found for one of the two stars, the search of the fringes for the second component gives the measure of the optical paths difference between the two fringe packets $\Delta\delta_{opt}(H)$ which are deduced the angular separation projected on the direction of the vector base at the time of the observation.

[6] http://www.mariotti.fr/litpro-page.htm

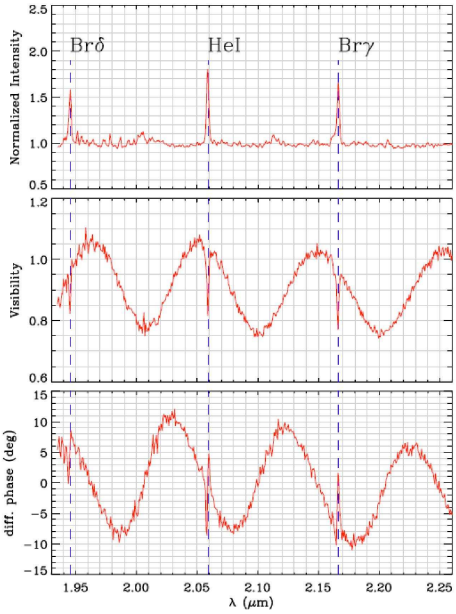

Fig. 13. Example of a spectrally resolved fringe visiblity measurements with VLTI/AMBER for one baseline in spectral medium resolution mode ($\frac{\lambda}{\Delta\lambda} = 1500$) in the K band. Oscillations due to the binarity of δ Sco are seen, as the three emission lines (Br δ, HeI 2.06 μm, and Br γ) produced by the circumstellar disc around the primary component (known as a Be Star). (From Figure 2 in Meilland et al. (2011))

So far we have left out the effect of the atmospheric turbulence (the seeing), a disturbing factor difficult to avoid during astronomical observations. In the case of Long Baseline Interferometry, the effect of the atmospheric turbulence occurs primarily at two levels. i) The random motion (tilt) and spreading (speckles) of the image making difficult the superposition of the light beams necessary for the formation of interference fringes. ii) The shifts of the arrival instants of the wavefronts on the two telescopes (piston effect) producing random variations in the length of the optical paths in the interferometer arms causes a random change $\sigma\delta_{opt}[atm]$ in the position δ_{opt} of the interference fringes is written then:

$$\delta_{opt} = \vec{B}_{sky} \,.\, \vec{S} + \sigma\delta_{opt}[atm] + c, \tag{4.14}$$

with $\vec{B}_{sky}$ the baseline vector, $\vec{S}$ the star vector (see Figure 8), and c an instrumental optical path difference precisely measurable using a metrology device.

In principle, the simultaneous observation of the two stars eliminates the disturbing term, but the observation procedure must satisfy the constraints related to the properties of atmospheric turbulence, namely:

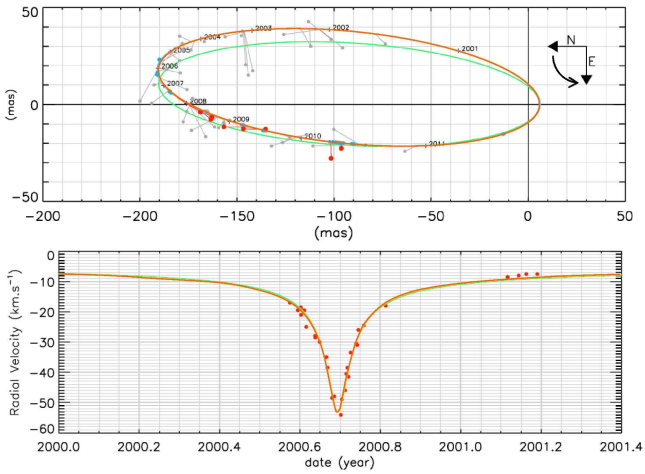

Orbital elements

P	=	10.811 ± 0.01 yr
T_0	=	2000.6941 ± 0.003
a''	=	98.74 ± 0.07 mas
e	=	0.9403 ± 0.0008
i	=	30.2 ± 0.7 °
ω	=	0.7 ± 2.9 °
Ω	=	174.0 ± 2.5 °
V_0	=	-6.7 ± 0.2 km s^{-1}
K_1	=	23.9 ± 0.1 km s^{-1}

Fig. 14. Top: Apparent orbit of δ Scorpii determined from AMBER/VLTI interferometric observations, from Figure 3 in Meilland et al. (2011). Red dots are measurements derived from VLTI/AMBER data, the blue ones from Tycner et al. (2011) and grey dots are the positions taken from de Fourth Catalog of Interferometric Measurements of Binary Stars. The green and blue solid lines represent the orbits derived by Tango et al. (2009) and Tycner et al. (2011) respectively. The VLTI/AMBER best-fit orbit is plotted as an orange solid line.
Middle: Radial velocitycurve of the primary component of δ Sco around the periastron from Figure 4 in Meilland et al. (2011). Data (red dots) are taken from Miroshnichenko et al. (2001). The green and orange lines represent Tango et al. (2009) and Meilland et al. (2011) orbits, respectively.
Bottom: δ Sco orbital elements of the visual and of the SB1 spectroscopic orbits as derived from VLTI/AMBER observations (Meilland et al., 2011).

- observe two stars closed enough on the sky so that the seeing can be considered identical on the two light beams (within the isoplanetic angle from about $2'' - 5''$ at $\lambda = 0.5\mu m$ to about $10'' - 30''$ at $\lambda = 2.2\mu m$),

- make the observation during a short time interval in order to consider the seeing as constant during the obervations (seeing lifetime to about $5 - 10ms$ at $\lambda = 0.5\mu m$ to about $20 - 50ms$ at $\lambda = 2.2\mu m$).

In these conditions, the difference in position between the two fringe packets can be written:

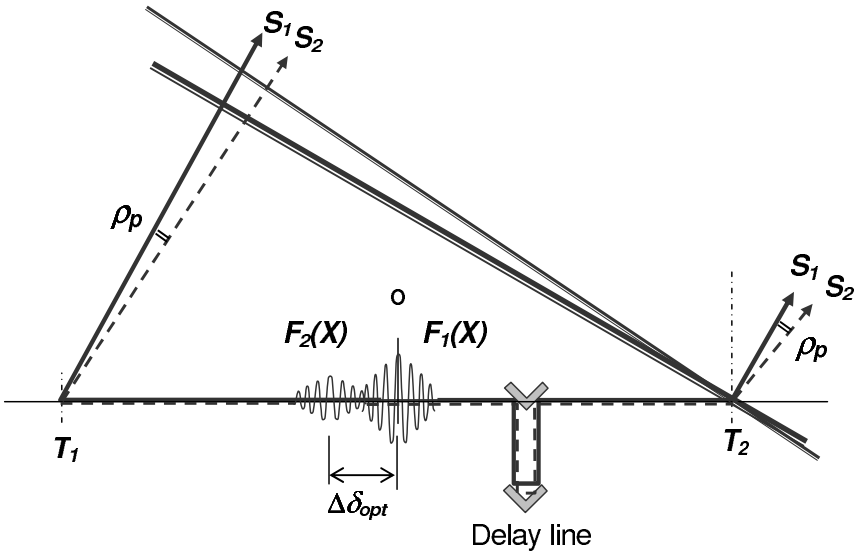

Fig. 15. Principe of the interferometric observation of a double star with the method of separated fringe packets.

$$\Delta\delta_{opt} = (\delta_{opt1} - \delta_{opt2}) = \vec{B}_{sky} \ . (\vec{S}_1 - \vec{S}_2) + (c_1 - c_2). \tag{4.15}$$

Note that a precision of $\sigma\rho_p = \pm 10\mu as$ in measuring a astrometric shift ρ_p requires accuracy $\sigma X = \pm 5nm$ in the measurement of the optical path length difference $\Delta\delta_{opt}$ between the stellar fringe packets.

The basic idea is to track the fringes simultaneously on the two stars in order to measure their separation ρ_p projected onto the baseline vector with an accuracy of the order of a fraction of the fringe spacing λ/B_{sky} and to achieve narrow angle differential astrometric observation with accuracy of the order of $10\mu as$ while the astrometric observations with long-focus telescopes were around $1mas$.

Separated Fringe Packets and *phase referenced interferometry* was proposed in the 1990's (Shao & Colavita, 1992; Quirrenbach et al., 1994b) and allow Narrow angle interferometric measurements of binary stars with the interferometers IOTA (Dyck et al., 1995), PTI (Lane & Colavita, 2003), and CHARA (Farrington et al., 2010).

The *Separated Fringe Packets interferometry* can be used if the stars are bright enough that the two fringe packets are detected with an exposure time shorter than the atmospheric coherence time. This constraint obviously limits the sensitivity of the interferometric observations. The *phase referenced interferometry* can be used to improve the sensitivity of the observations. In this technique, the fringes of a bright star are used to measure the fringe phase fluctuations induced by atmospheric turbulence in order to correct, in real time, the fringe phase on the fainter companion which are then detected with an exposure time longer than the atmospheric coherence time.

The application of this technique is illustrated by the observation of the binary ADS 11468 AB (A 1377, HD 171779, K0 III + G9 III, $m_V = 5.37$, $\Delta m_V = 0.21$, $m_K = 2.78$) made with the North-South 110 m baseline of the PTI interferometer in a spectral band of $\lambda = 2.2\ \mu m, \Delta\lambda = 0.40\ \mu m$. For details see Lane & Muterspaugh (2004).

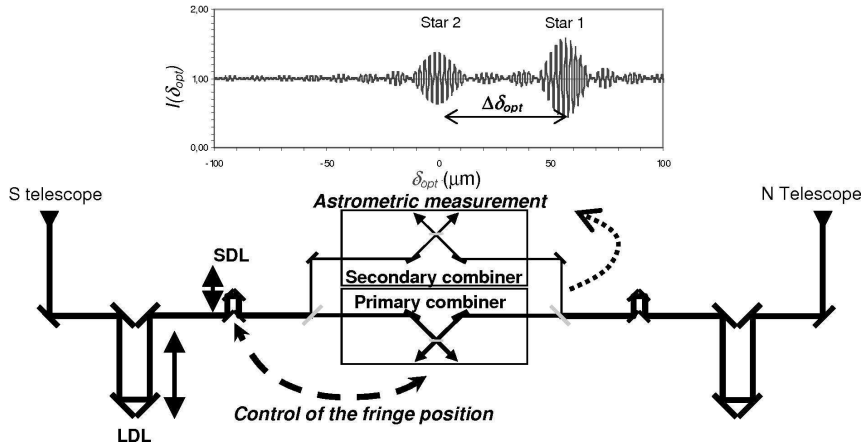

Fig. 16. Schematic diagram of the PTI instrumental configuration for Separated Fringe Packets or Phase referenced interferometric observations. Long delay lines (LDL, optical delay $\pm 38.3m$) and short one (SDL, optical delay $\pm 3cm$) placed on the southern arms of the interferometer are active during the observation for the control of the position of the interference fringes tracked with the primary combiner. The astrometric measurement is performed by the secondary combiner.

Figure 16 shown the schematic diagram of the PTI instrumental configuration for Separated Fringe Packets or Phase referenced interferometric observations (Lane & Colavita, 2003). The primary fringe tracker allows to find the fringes by adjusting the optical path difference with the long delay line (LDL) and then measures the random fluctuations of the fringes position (or fringe phase) produced by the atmospheric turbulence by scanning the optical path length with an amplitude modulation of 1 λ, and a frequency of $\approx 100\ Hz$. The error signal controls the short delay line (SDL) in order to fix the position of the fringes, with a frequency of the control loop of $\approx 10\ Hz$. The secondary fringe tracker saves stable fringes by modulating the optical path difference with an amplitude modulation of $\approx 500\ \mu m$, a frequency $\approx 1\ Hz$ and integration time 50, 100 or 250 ms. It allows to record the two fringe packets to obtain differential astrometric measurement of the two stars.

Figure 17 shows an example of the double fringes packets recorded by controlling the position of the fringes by primary tracker fringe (exposure time 10 ms, the correction optical path difference 10 times per second) and performing the astrometric measurement with secondary fringe tracker (amplitude $\pm 150\ \mu m$, period 3 s). Note that the recorded signal is disturbed by the presence of noise in part due to imperfect correction of the effects of atmospheric turbulence. Each scan is analyzed to obtain a measurement of the differential delay by fitting on the data an astrometric model with two free parameters

(ρ, θ) or $(X = \Delta\alpha \cos\delta, Y = \Delta\delta)$.

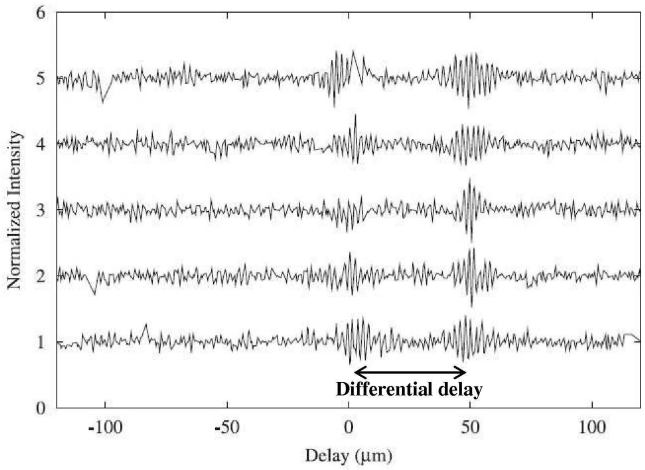

Fig. 17. Five consecutive records fringes on the visual double star ADS 11468 AB. The exposure time of each record is 1.5 s. (From Figure 3 in Lane & Muterspaugh (2004))

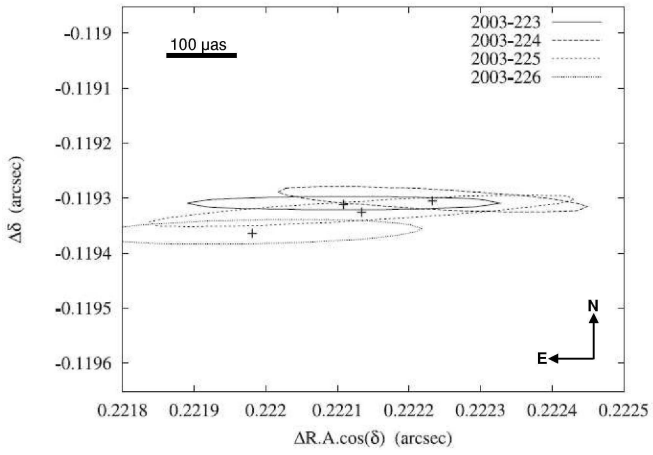

Fig. 18. Five consecutive records fringes on the visual double star ADS 11468 AB. The exposure time of each record is 1.5 s. (From Figure 3 in Lane & Muterspaugh (2004))

Figure 18 shown that for four consecutive nights from 11th to 14 August 2003, these observations have identified the relative position (X, Y) between the components (Figure Y) by fitting a simple model of interferometric binary signal on the interferometric signal measured after correction for known instrumental effects. The angular separation $\rho = 0.252158\ ''$position and angle $\theta = 118.32^{\ o}$ calculated from the mean values

$< X >= -0.119324\,''$ and $< Y >= 0.222138\,''$ are in good agreement with the values $\rho = 0.248\,''$ and $\theta = 120.9^{\,o}$ predicted from the orbit period P = 191.49 years. The uncertainties of the astrometric differential interferometric measurements, $\sigma X \sim 144 - 143\,\mu as$ and $\sigma Y \sim 8 - 12\,\mu as$ are highly anisotropic due to the fact that the angular resolution of a North-South baseline interferometer is actually only achieved in the direction of the north-south component of the projected sky baseline (hence following the declination δ), while in the perpendicular direction (that of the right ascension α) the angular resolution remains fundamentally limited by the short length of the east-west component of the projected sky baseline produced by the Earth's rotation. The main conclusion remains i.e. the errors on the interferometric measurement are about 10 to 100 times lower than those of other techniques.

5 Separation of the spectra of the binary components

Using spectro-interferometric instruments one can measure the visibility and phase variation as function of the wavelength. As seen in the section 4.1, this can be used to enhance the (u,v) plan coverage of some observation as the spatial frequency is defined by $\overrightarrow{B}/\lambda$. However, this assumes that the object intensity distribution is achromatic. If the object intensity distribution depends on the wavelength, the spectral variations of the visibility and phase are a mix of effects from the spatial frequency variation and the wavelength dependency of the object.

In the simplest case of an unresolved binary star, the object wavelength dependence is only due to the variation of the flux ratio between the two stars. We can rewrite Equation 4.9:

$$V(B,\lambda) = \frac{1}{1+R(\lambda)}\sqrt{1+R(\lambda)^2+2R(\lambda)\cos\left(\frac{2\pi\overrightarrow{\rho}\overrightarrow{B}}{\lambda}\right)}, \tag{5.1}$$

where $R(\lambda)$ is the wavelength dependent flux ratio between the two components of the system. This chromatic parameter mainly influence the variation of the visibility modulation amplitude. It can easily be constrained using model fitting techniques. Moreover, if the total normalized spectrum $S(\lambda)$ can be measured by the spectro-interferometric instrument or by an other instrument, the relative spectra of each component can be determined easily.

Using such technique Chesneau et al. (2014) managed to separate the spectrum of the interacting binary HR 5171 A (Fig 19). In that case the authors were able to show that the CO emission seen in the total spectrum originates from the circumstellar environment and that the primary was showing CO lines in absorption as expected from its inferred spectral class.

Using a similar technique one can reconstruct the spectral energy distribution (SED) of multi-component objects using interferometric measurements in various spectral bands and photometric or spectro-photometric measurements. Such methods allow to put constraints on the physical parameters of each component of the system. A nice example showing the possibility of such technique is the work done by Millour et al. (2009a) on the unclassified B[e] HD 87643. Using AMBER and MIDI measurements the authors

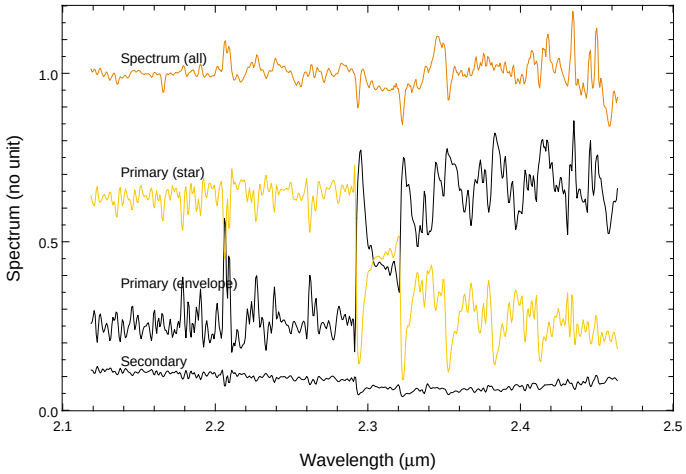

Fig. 19. Separation of the medium-resolution K band spectra HR5171 A based on analysis of VLTI/AMBER data using geometric models. The upper orange line is the full AMBER spectrum. The yellow line is the spectrum from the uniform disk which its respective normalized flux. The contribution from the Gaussian is characterized by the strong CO emission lines, and the secondary flux is the bottom line at about 12% level in the continuum. From Chesneau et al. (2014).

managed to detect the binarity of this object surrounded by a large circumbinary environment. They also constrained the variation of the flux ratios between the three components of the object (the two stars and the envelope) from 1.6 to 13μm. Finally, using some photometric measurements from the literature for the visible and near-infrared, and using the IRAS and MIDI spectro-photometric measurements in the mid-infrared they manage to separate the SEDs from the primary, the secondary and the cirumbinary envelope. As seen in Fig 20 they roughly derived the temperature of each component, and they showed that secondary was highly embedded and that the N-band silicate emission was mainly coming from the large circumbinary envelope.

Finally, if the (u,v) plan coverage is well sampled and the observations are performed with a spectro-interferometric instrument, spectrally-resolved images can be reconstructed (see Chapter I). In that case the reconstructed data is very similar to those of integral field spectroscopy but with a much higher spatial resolution. Such technique as not been used yet on multiple stars to directly separate the fluxes of the different component of the system, but it was successfully applied to disentangle the stellar and circumstellar emissions of the Be star ϕ Per (See Chapter III).

6 When double stars interact

As mentioned in the introduction of this chapter, many double stars cannot be simply regarded as two single stars orbiting around a common center of mass. This is only the case of wide double star whose components are subject to only their gravitational attractions but continue their evolutions as isolated stars. This is no longer the case of

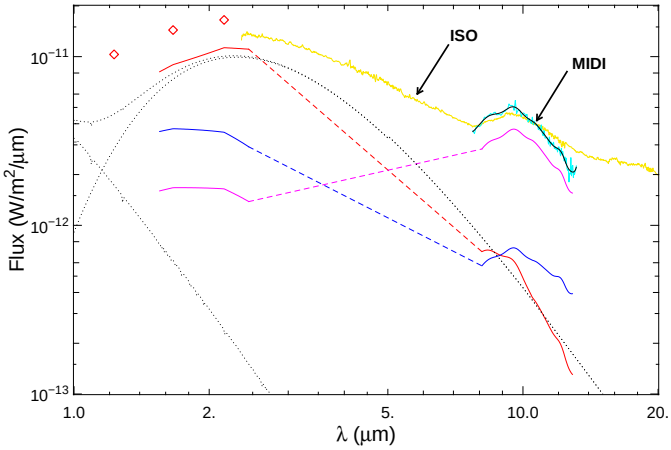

Fig. 20. The (non-de-reddened) HD 87643 SED with the extracted fluxes from VLTI/AMBER and VLTI/MIDI interferometric measurements. The southern component flux is shown in red (top curve at 2 m), the northern component flux is shown in blue (middle curve at 2 m), and the resolved background flux is shown in pink (bottom curve at 2μm). The dotted lines correspond respectively to a Kurucz spectrum of a B2V star and to a black-body flux at 1300 K, for comparison. From Millour et al. (2009a)

close binaries when the separation between the two components decreases so that the evolution of each is influenced by the presence of the companion.

Depending on the degree of interaction between components, close double stars are classified as detached, semi-detached, contact, and common-envelope systems and are all considered as interacting binaries. The type of interaction depends on the physical properties of stars: if at least one of the components fills its Roche lobe, gravitational interactions mainly occurs, characterized by mass transfer and the presence of a circumstellar or circumbinary accretion disk. For massive binary stars, are observed not only stellar components, but also phenomena produced by the interaction between the hot and dense stellar winds and sometimes jet structures which are an indication of a mass loss by the binary system.

For the study of the complex morphology of the objects, high angular resolution observations by long baseline optical interferometry are needed in addition to information provided by the spectroscopic and photometric observations

6.1 Gravitational interactions

In close binary systems a component can have a part of its mass accreted by the most massive component and this may affect the stellar surfaces. To understand the possible effects, one has to take into account the gravitational forces of both components and the centrifugal forces induced by the rotation of the two stars around their centre of mass. The energy potential of such system, called Roche potential after the French Astronomer Edouard Roche, is given by:

$$\Phi(\vec{r}) = -\frac{GM_1}{\left|\vec{r}-\vec{r_1}\right|} - \frac{GM_2}{\left|\vec{r}-\vec{r_2}\right|} - \frac{1}{2}\left|\vec{\omega}\times\vec{r}\right|^2, \tag{6.1}$$

where M_1 and M_2 are the masses of the two stars, $\vec{r_1}$ and $\vec{r_2}$ their respective positions, and $\vec{\omega}$ the system angular velocity. Fig 21 illustrate the Roche equipotentials and shows the five Lagrangian points (L_1 to L_5) defined by $\nabla\Phi$=0. The Roche lobes of the system are defined by the equipotential that contains L_1. The equipotentials of higher energy are separated for each star, whereas those of lower energy are merged into a single "peanut" shape surface.

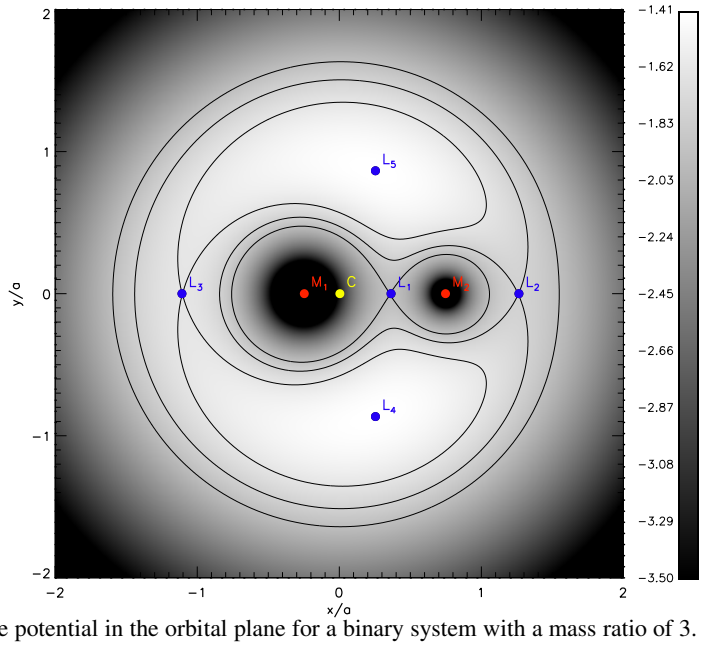

Fig. 21. Roche potential in the orbital plane for a binary system with a mass ratio of 3. The spatial scale is normalized by the system major-axis a. The position of the two stars are note M_1 and M_2, the center of Mass, C, and the five Lagrangian points L_1 to L_5. The equipotentials going through L_1 to L_3 are shown as a solid line.

In the absence of other forces, these equipotentials define the possible surfaces of the two stars. For a small-enough stars compared to the binary separation, the gravitational effect of the companions is negligible and the stellar surfaces are spherical as shown by the high energy equipotential. For larger stars, i.e. lower energy, the surface starts to be influenced by the companion and its shape starts to differ from a sphere and to look like a pear. Nevertheless, in both cases, the system is called "detached" as there is no mass-transfer between the components. In a "semi-detached" system, one of the two components completely fills its Roche lobes, and matter can easily flow from L_1 into the Roche lobe of the other component, usually spiralling down to the star, and forming an accretion disk around it. If both stars fill their respective Roche lobe, the system will be "in-contact", with the contact occurring at L_1. Beyond that point, the two stars can form

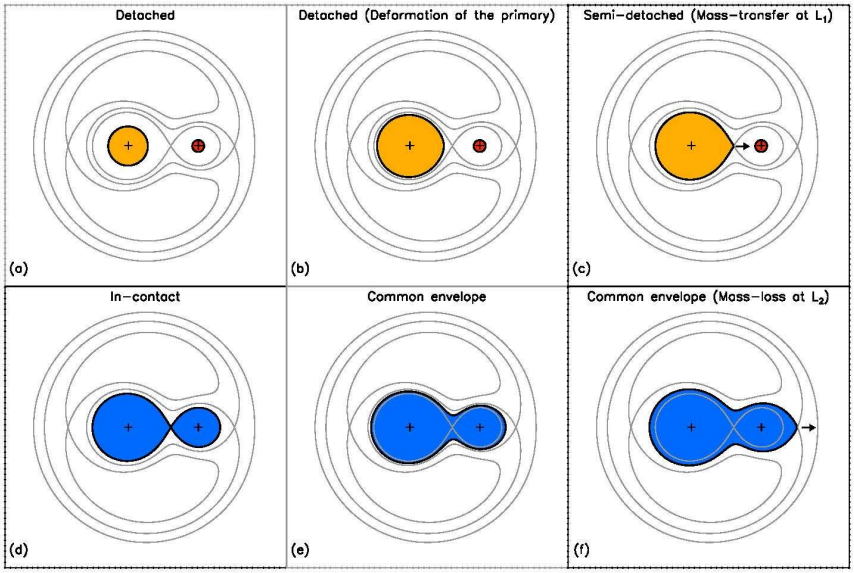

Fig. 22. Six different cases of close binary systems. The Roche equipotential from Fig 21 are overplotted as solid grey lines. The arrows represent the possibility of mass-transfer or mass loss in the case of the semi-detached and common-envelope phases.

We note that, as components of binary systems evolve on the main sequence and beyond, they can go through these different phases. Moreover, the mass-transfer that occurs during the semi-contact phase can strongly influence the stellar evolution of both components as is the mass-loss occurring in the common-envelope phase. Finally, the rotation of the outer layer of the stars can also be strongly influenced by the companion. For instance, a star in a semi-detached phase will be spin-up by tide-effect from the companion. Moreover, outer layers of system in the in-contact or common envelope phases are supposed to be co-rotating, i.e. rotating at the Keplerian velocity, far above the typical velocity of evolved stars.

Interferometry is a well-suited technique not only to constrain the projected orbit of interacting binaries but also to probe the geometry of their stellar surfaces and often complex circumstellar environment. An example of a well studied system is β Lyr, a semi-detached binary whose secondary is surrounded by a accretion disk. First observations performed with the GI2T interferometer in the Hα emission line were published in Harmanec et al. (1996). They showed that the gaseous emission was stemming from an environment larger than the binary separation, and that part of it could comes from jet-like structures perpendicular to the orbital plane. This hypothesis was confirmed by recent CHARA/VEGA observations (Bonneau et al., 2011). In this paper the authors also studied the case of

another interacting binary, ν Sgr, showing that the Hα emission was more likely coming from a circumbinary disk, probably fed by mass-loss flowing from L_2. β Lyr was also studied in the near-infrared using the CHARA/MIRC instrument (Zhao et al., 2008). The author observed the system at different epochs and managed to reconstruct images at the corresponding phases of the orbit (see Fig 23). They constrained the orbital parameters, and partly resolved the two components, showing that the primary was distorted due to the Roche lobe filling and the emission of the secondary is stemming from the almost edge-on accretion disk.

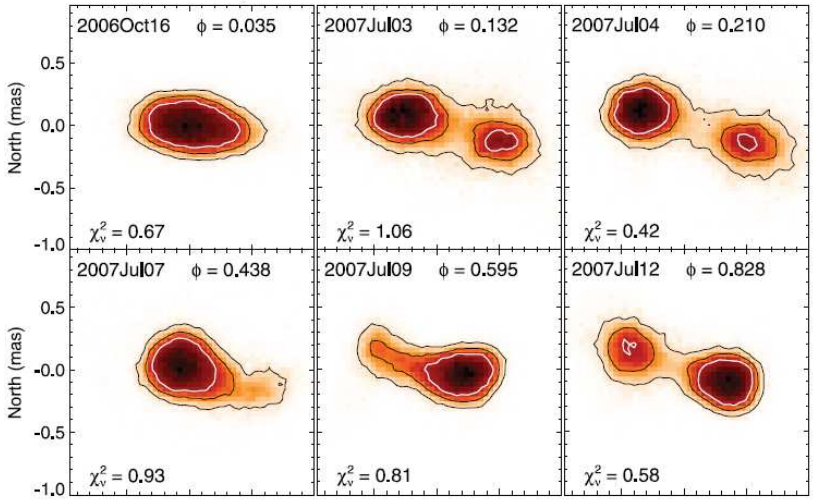

Fig. 23. Images of β Lyr reconstructed at different epoch of the orbit using CHARA/MIRC data. From Zhao et al. (2008).

The interferometric characterization of stellar distortion induced by binarity is not trivial. As the distortion is small, i.e. a few percent of the stellar diameter, very accurate measurements, and a decent (u,v) plan coverage including baselines long enough to fully resolve the primary, are needed to achieve this goal. For instance, Blind et al. (2011) did not managed to derive the distortion of the primary in SS Lep symbiotic system using VLTI/PIONIER measurement. However, they managed to derive the mean diameter of the primary, showing that it was not filling the Roche Lobe and that the measured mass transfer was more likely to occur through the capture of a part of the primary stellar wind. This result was confirmed by Boffin et al. (2014) on three of the six symbiotic stars that they observed with the VLTI/PIONIER instrument. For these three objects, the authors found a filling factor of the Roche Lobe of the order of 0.5-0.6, whereas they found clues of elongation and a filling factor close to 1 for the three others stars.

Interferometry also allowed to discover the binary nature of one of the most extended star of the galaxy, the yellow hypergiant HR 5171 A (Chesneau et al., 2014). VLTI/AMBER data revealed the presence of a very close companion that was located at the limb of the primary disk during the observations (see Fig 24). A detailed study of

the photometric variation of the stars confirmed the binarity of the system that the star was in a in-contact for common envelope phase. Finally, a careful analysis of the spectrum, confirmed that the primary surface was rotating close to the breakup velocity as expected for close binaries in common-envelope phase.

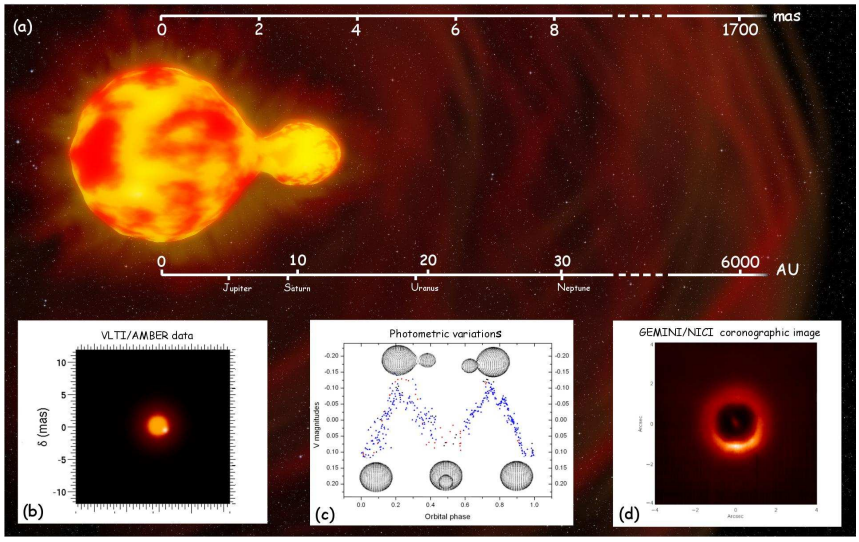

Fig. 24. (a) Artist view of HD 5171 A. (b) model of the VLTI/AMBER data. (c) photometric variations. (d) GEMINI/NICI large scale coronographic image. From (Chesneau et al., 2014).

Tide effects from a close companion can also affect the circumstellar environment of the primary. For instance, this is the case of some classical Be stars. If the ellipticity is small and the stellar equator and orbit are co-planar, the companion might simply truncate the disk as for ζ Tau (Quirrenbach et al., 1994a) or ϕ Per (Mourard et al., 2014). For a highly elliptic orbit with a close-enough periastron, the circumstellar disk around the primary is likely to be perturbed by the companion during the periastron passage. For instance, this is the case of δ Sco (Che et al., 2012; Meilland et al., 2013). Finally, if the orbital and stellar equatorial plane are not coplanar, the tide effects can torque the disk.

Disk and companion interaction are not fully understood yet. For instance, although most of the stars showing the B[e] phenomenon are found to be binaries, the mechanisms leading to the formation of a dense equatorial disk is not yet understood. In the case of these hot and massive stars, one as to take into account, not only the gravitational interaction between the components, but also some possible wind-wind collision or wind capture by the companion.

HD 62623, the coldest star showing the B[e] phenomenon was observed with the VLTI instruments MIDI (Meilland et al., 2010) and AMBER (Millour et al., 2011). These observations show that the star is surrounded by a stratified gaseous and dusty disk. Constraints on the inclination angle show that the star is rotating too slow for the bi-stable mechanism (Lamers & Pauldrach, 1991) to explain the disk formation, but too fast for a supergiant

star. The companion, not detected in the interferometric data but located in the disk, could have spin-up the primary as for HR 5171 A. The disk may be a residual from a previous interaction.

6.2 Shock interactions

Wind interactions When two hot massive stars in a pair interact, there is no accretion, due to the fast and dense radiation-driven winds. Indeed, these winds are accelerated by the "line blanketing" effect (i.e. the numerous interactions of photons with the many broadened lines the gaz offers to the luminous flux from the star). Instead, their winds crash onto each other, producing a bow-shock and a wealth of associated phenomena.

Depending on the energy of the shock, UV, X-Rays or even sometimes Gamma-Rays can be emitted in the region of the shock. These energetic radiations participate to the ionization of the surrounding gazeous regions, hence producing free-free emission (continuum) and line emission. This additional emission may be detected by means of interferometric observations, e.g. for γ Velorum for the free-free emission (Millour et al., 2007). In other cases, there is only indirect evidence of the shock due to the highly eccentric orbit of the secondary star, or the presence of dust in the system which veils some of the shock clues. This is for example the case of Eta Carinæ.

Finally, the region of the shock is a heavily turbulent, dense, and slow region between the winds of the two stars, which are somewhat less dense medium, faster and a strong radiation source. Somewhere in the shock, due to these ingredients, the metallic ions condense into dust, which form an expanding plume of material. This plume has a very characteristic shape (see Fig. 25) named a "pinwheel" nebula. This is for example the case of the candidate Gamma Ray burst binary star WR104 (Monnier et al., 2007), or another dusty Wolf-Rayet star WR140 (Monnier et al., 2002). For such system, the naked binary star model does not match the data, and specific models like in Harries et al. (2004) or (Millour et al., 2009b) need to be developed.

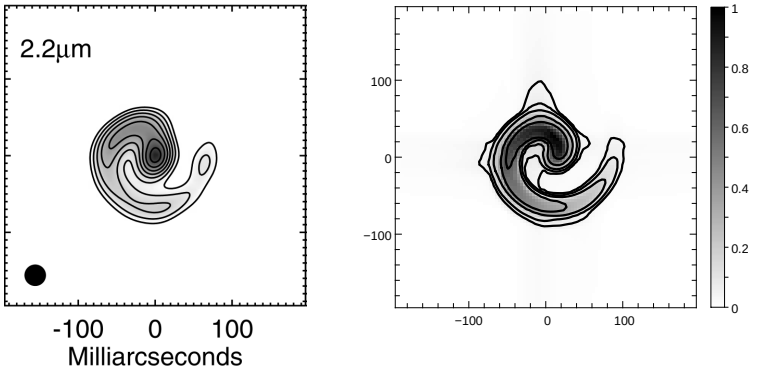

Fig. 25. Left: Figure from (Monnier et al., 2007) showing the "pinwheel" nebula around the Wolf-Rayet star WR104 in the near infrared. **Right:** The same model as in Millour et al. (2009b) with parameters that make the image similar to WR104 image.

Cataclysmic binaries Cataclysmic binaries are made of a white dwarf (WD, receiver) and a main-sequence or giant star (donnor). A mass transfer (accretion) from the donnor to the receiver occurs through the Roche lobe contact at the Lagrange points.

As a consequence, the WD surface gains mass until it reaches the thermonuclear ignition mass, causing it to explode explode in a thermonuclear runaway (TNR). This results in a brightening of 7 to 15 magnitudes called a Nova. Once the explosion has vanished, the cycle of mass-gaining/TNR can start again with a typical period of 10^4 years.

At each growth/TNR cycle, the white dwarf gains a little mass, making accelerate the cycle time. Therefore, some novae have cycles with periods as small as 10 years. These novae are called recurrent novae. The very short timescale of recurrence indicates a WD close to the Chandrasekhar limit, making it a candidate for Type Ia supernovae.

The work done on Novae with interferometry is well-synthesised in the review of Chesneau & Banerjee (2012). It started in 1992 with Nova Cygni 1992 observed with the Mk III interferometer, and until now, almost all bright novae were observed using one or the other interferometric facilities available (VLTI, PTI, CHARA, etc.).

The main conclusion from these studies is that the novae ejecta are not spherical, as was previously considered. This is even the case just a few days after the outburst (Chesneau et al., 2007, 2011), indicating that the ejecta shaping occurs already at the earliest phases of the nova explosion and not with later interactions with the ISM. This has strong implications on the determination of the distance of the system using spectroscopic parallax estimates, as demonstrated in Schaefer et al. (2014).

References

Armstrong, J. T., Mozurkewich, D., Vivekanand, M., et al. 1992, AJ, 104, 241

Blind, N., Boffin, H. M. J., Berger, J.-P., et al. 2011, A&A, 536, A55

Boffin, H. M. J., Hillen, M., Berger, J. P., et al. 2014, A&A, 564, A1

Bonneau, D., Chesneau, O., Mourard, D., et al. 2011, A&A, 532, A148

Che, X., Monnier, J. D., Tycner, C., et al. 2012, ApJ, 757, 29

Chesneau, O. & Banerjee, D. P. K. 2012, Bulletin of the Astronomical Society of India, 40, 267

Chesneau, O., Meilland, A., Banerjee, D. P. K., et al. 2011, A&A, 534, L11

Chesneau, O., Meilland, A., Chapellier, E., et al. 2014, A&A, 563, A71

Chesneau, O., Nardetto, N., Millour, F., et al. 2007, A&A, 464, 119

Davis, J. 2007, in IAU Symposium, Vol. 240, IAU Symposium, ed. W. I. Hartkopf, P. Harmanec, & E. F. Guinan, 45–53

Duchêne, G. & Kraus, A. 2013, Annual Rev. of Astron. & Astrophys., 51, 269

Dyck, H. M., Benson, J. A., & Schloerb, F. P. 1995, AJ, 110, 1433

Farrington, C. D., ten Brummelaar, T. A., Mason, B. D., et al. 2010, AJ, 139, 2308

Finsen, W. S. 1934, Circular of the Union Observatory Johannesburg, 91, 23

Guinan, E. F., Harmanec, P., & Hartkopf, W. 2007, in IAU Symposium, Vol. 240, IAU Symposium, ed. W. I. Hartkopf, P. Harmanec, & E. F. Guinan, 5–16

Harmanec, P., Morand, F., Bonneau, D., et al. 1996, A&A, 312, 879

Harries, T. J., Monnier, J. D., Symington, N. H., & Kurosawa, R. 2004, MNRAS, 350, 565

Hartkopf, W. I., McAlister, H. A., & Mason, B. D. 2001, AJ, 122, 3480

Heintz, W. D. 1978, Geophysics and Astrophysics Monographs, 15

Kovalevsky, J. 1995, Modern Astrometry (Springer-Verlag)

Lamers, H. J. G. & Pauldrach, A. W. A. 1991, A&A, 244, L5

Lane, B. F. & Colavita, M. M. 2003, AJ, 125, 1623

Lane, B. F. & Muterspaugh, M. W. 2004, ApJ, 601, 1129

McAlister, H. A. 2007, in IAU Symposium, Vol. 240, IAU Symposium, ed. W. I. Hartkopf, P. Harmanec, & E. F. Guinan, 35–44

Meilland, A., Delaa, O., Stee, P., et al. 2011, A&A, 532, A80

Meilland, A., Kanaan, S., Borges Fernandes, M., et al. 2010, A&A, 512, A73

Meilland, A., Stee, P., Spang, A., et al. 2013, A&A, 550, L5

Millour, F., Chesneau, O., Borges Fernandes, M., et al. 2009a, A&A, 507, 317

Millour, F., Driebe, T., Chesneau, O., et al. 2009b, A&A, 506, L49

Millour, F., Meilland, A., Chesneau, O., et al. 2011, A&A, 526, A107

Millour, F., Petrov, R. G., Chesneau, O., et al. 2007, A&A, 464, 107

Miroshnichenko, A. S., Fabregat, J., Bjorkman, K. S., et al. 2001, A&A, 377, 485

Monnier, J. D., Tuthill, P. G., & Danchi, W. C. 2002, ApJL, 567, L137

Monnier, J. D., Tuthill, P. G., Danchi, W. C., Murphy, N., & Harries, T. J. 2007, ApJ, 655, 1033

Mourard, D., Monnier, J. D., Meilland, A., et al. 2014, submited to A&A

Pourbaix, D. 1994, A&A, 290, 682

Pourbaix, D. 1998, A&AS, 131, 377

Quirrenbach, A., Buscher, D. F., Mozurkewich, D., Hummel, C. A., & Armstrong, J. T. 1994a, A&A, 283, L13

Quirrenbach, A., Mozurkewich, D., Buscher, D. F., Hummel, C. A., & Armstrong, J. T. 1994b, A&A, 286, 1019

Rosvick, J. M. & Scarfe, C. D. 1991, MNRAS, 252, 68

Sana, H., de Mink, S. E., de Koter, A., et al. 2012, Science, 337, 444

Schaefer, G. H., Brummelaar, T. T., Gies, D. R., et al. 2014, Nature, 515, 234

Shao, M. & Colavita, M. M. 1992, A&A, 262, 353

Siess, L., Izzard, R. G., Davis, P. J., & Deschamps, R. 2013, A&A, 550, A100

Tango, W. J., Davis, J., Jacob, A. P., et al. 2009, MNRAS, 396, 842

Tycner, C., Ames, A., Zavala, R. T., et al. 2011, ApJL, 729, L5

Zhao, M., Gies, D., Monnier, J. D., et al. 2008, ApJL, 684, L95